Science
AAAS

Supplementary Materials for

More extreme Indian monsoon rainfall in El Niño summers

Spencer A. Hill *et al*.

Corresponding author: Spencer A. Hill, shill1@ccny.cuny.edu

Science **389**, 1220 (2025)
DOI: 10.1126/science.adg5577

The PDF file includes:

Materials and Methods

Region definitions

The four subregions of India are those used by ref. (*6*). The "All Monsoonal India" (AMI) region comprises all gridpoints in the monsoonal India domain defined by ref. (*31*). The remaining three are non-overlapping subsets of AMI. The Central Monsoon Zone (CMZ) definition also follows ref. (*31*), spanning from Pakistan to the Bay of Bengal in a wide band north of peninsular India. The Western Ghats (WG) region is defined as all land points within the polygon whose vertices are (76.5°E, 7.5°N), (78.5°E, 7.5°N), (74°E, 18°N), (74°E, 21.5°N), (72.25°E, 21.5°N), and (72.25°E, 18°N). The Southeast India (SEI) region includes all points south of 18°N that are not within WG. The WG and SEI region borders were defined by (*6*) explicitly based on JJAS-mean rainfall properties in the India Meteorological Department 0.25° dataset to distinguish the coherent regimes within peninsular India, but neither they nor the other regions were defined explicitly with reference to extreme rainfall characteristics.

Region-aggregated distributions are computed by combining fields from all gridpoints of a given region into a single distribution without any area weighting. Region-averaged fields are area-weighted averages across all gridpoints within each region.

India Meteorological Department $0.25° \times 0.25°$ rainfall dataset

Daily rainfall data comes from the 0.25°×0.25° latitude-longitude gridded product produced by the India Meteorological Department (IMD) (*30*). This dataset spans all days of the year from January 1, 1901 to the present, and we use all days in June, July, August, and September (JJAS) from 1901 through 2020. This gridded product is derived from a dense network of in situ rain gauges with coverage throughout India, using a simple interpolation procedure to go from the irregular station coverage to the regular latitude-longitude grid. The rain gauge coverage varies in time, with ~1500 stations in 1901, peaking above 4000 stations in the early 1990s, and then decreasing appreciably to ~2000 in the 2010s (*30*). These secular trends in station coverage have been argued to strongly influence inferences about long-term trends in daily rainfall extremes (*35*). For our purposes, however, for interannual variability it is unlikely that the fluctuations in station coverage would alias onto ENSO.

This dataset contains spurious values in a few gridpoints and times, which appear to us to stem from errant reported values from one or more stations which then propagate in space through the interpolation procedure. In particular, in northeast India directly along the border with Bangladesh, starting in the 1970s values become implausible, as shown in Fig. S1. We mask these out along with the rest of northeastern and far northern India as part of our "monsoonal India" mask (*31*). As discussed by ref. (*31*), the masking of northern India is due to insufficient data in the Himalayan foothills. Nevertheless, the density of rain gauges dating back to the 19th century and the stewardship of the resulting data by the India Meteorological Department make this an extremely high-quality dataset.

India Meteorological Department $1^\circ \times 1^\circ$ rainfall dataset

We have replicated all key analyses on the India Meteorological Department's $1^\circ \times 1^\circ$ gridded product (*34*). This product uses the same interpolation procedure of India Meteorological Department station data, but in addition to being coarser, it differs from the 0.25° product in that its network of 1,803 stations is fixed in time. There are no substantive discrepancies in our key findings between the two products. Perhaps most notable is that daily rainfall values within the very narrow WG coastal band reach considerably larger values in the higher-resolution product, which is reflected in the WG region-aggregated daily cutoff (Fig. 2b). But this amounts to a approximately constant offset; the ENSO signals in this and other regions are similar between the two products. The overall consistency of results between the 0.25° and 1° datasets bolsters confidence that the interannual signals we document are not strongly influenced by changes in the station network in time used by the 0.25° dataset—which, conversely, does strongly influence secular trends (*35*).

Cutoff rain rate

We compute the cutoff daily rain rate using the method of moments, which for a given daily rainfall distribution is simply the variance divided by the mean. This measure is motivated by the correspondence of daily rainfall distributions to gamma distributions (*29*). In terms of shape parameter k and scale parameter θ, the gamma probability density function, $f(x)$, follows $f(x) \propto x^{k-1}e^{-x/\theta}$, from which the cutoff is easily identified as the scale parameter θ. Moreover, for gamma distributions the variance is exactly $k\theta^2$ and the mean is $k\theta$. Thus, insofar as the daily rainfall distributions

approximately follow gamma distributions, the variance-to-mean ratio usefully estimates the cutoff.

The method of moments is easily calculated, but being computed over the entire distribution, it is influenced by behavior at the low end of the daily rainfall distribution as well as the extremes. Given the strong influence of ENSO on no- and low-rainfall day frequencies, this potentially makes it a biased metric of extremes. We have tested the sensitivity to behaviors at low rain rates by computing it restricting to rain rates over different thresholds. This increases the mean of the remaining sample, yielding a low-biased cutoff estimate, but results in terms of correlations with NINO3.4 or ratios of ENSO composite quantities are qualitatively insensitive.

An alternative method for computing the cutoff is via a linear regression of the daily rainfall PDF in semi-log space (*56*). Denoting the daily rainfall PDF as $f(P)$, a linear regression is performed of $\log(f(P))$ on P but restricting to the right tail of the distribution (which, being quasi-exponential, is close to a straight line); denoting the slope of this regression r, the cutoff estimate is then $-1/r$. While this avoids contamination by the low end of the distribution, we find it strongly determined by the few largest values: for the parameter choices explored, we find the regional cutoffs for each JJAS computed via the regression to all be correlated at $r > 0.9$ with the region's JJAS block maximum rain, compared to $r \sim 0.5 - 0.7$ with the method of moments.

As such, we elect to use the cutoff computed from the method of moments, taking it to be more representative of behaviors throughout the right tails of the daily rainfall distributions.

NINO3.4 index

As our index of ENSO, we compute the standard NINO3.4 index of sea surface temperature (SST) anomalies averaged over the central and eastern equatorial Pacific: 120°–170°W, 5°S–5°N. The monthly SSTs come from the National Oceanic and Atmospheric Administration Extended Reconstructed SST (ERSST) dataset, version 5 (*57*). The SSTs are first averaged with area-weighting over the NINO3.4 region for each month. They are then averaged over JJAS for each year. The linear trend computed by least squares regression over 1901-2020 of this timeseries of JJAS values is then computed and subtracted off. Finally, the time mean of this detrended timeseries is computed and subtracted off to generate an anomaly timeseries; the result is the NINO3.4 index we use.

We have also repeated key calculations using JJAS deviations of the NINO3.4 averaged SSTs from a 30-year rolling mean with no detrending, more akin (but not identical) to the NOAA

Oceanic Niño Index (ONI), finding little sensitivity. For example, the region cutoffs for each JJAS are correlated with ONI at $r = 0.29, 0.29, 0.19$, and -0.19 for AMI, CMZ, WG, and SEI, respectively, all less positive but within 0.05 of the corresponding correlations using NINO3.4.

Detrending

The trend for each field is computed via least-squares regression in time over 1901-2020. De-trended fields are constructed by subtracting this trend from the full field. All correlation coefficients are computed on fields linearly detrended in this way.

ENSO composites

For ENSO-based composites, we use a ±0.3 K threshold of the NINO3.4 index: all summers w/ JJAS NINO3.4 exceeding +0.3 K are designated El Niño, those between -0.3 and +0.3 neutral, and those less than -0.3 La Niña. These -0.3 and +0.3 threshold values correspond to the 34th and 70th percentiles of the JJAS NINO3.4 distribution respectively. Results appear insensitive to this threshold from values of 0 to roughly ±1.0. For example, the AMI composite cutoffs for a 0 K threshold are 36.7 and 33.8 mm respectively for El Niño and La Niña; for a ±1 K threshold they are 36.4 and 33.5 mm, respectively, with only small fluctuations for intermediate values. The ±0.3 K threshold was subjectively chosen as a compromise between maximizing the sample size of each composite vs. maximizing the difference in the large-scale atmospheric state between the composites.

Risk ratios

To compute the ENSO risk ratio for a given field, first we compute the empirical cumulative distribution function (CDF, denoted $F(x)$) for that field for the El Niño composite and separately for the La Niña composite. By definition of the CDF, in either composite, the empirical probability of exceeding a given value equals one minus the CDF at that value: $P(X \geq x) = 1 - F(x)$. As such, the ENSO risk ratio is computed as $(1 - F_{\mathrm{EN}}(x))/(1 - F_{\mathrm{LN}}(x))$, where the subscripts "EN" and "LN" refer to El Niño and La Niña respectively. We compute risk ratios in this manner for daily rain accumulation on rainy days (using a standard >1 mm threshold), computing it separately for

each of our four regions.

Statistical significance estimates

For the statistical significance of the pointwise correlations, we employ a False Discovery Rate technique (*58*), which accounts for the fact that given many individual gridpoints, some of the nominally significant points based on local tests will likely be spurious. First, a p value is computed for each gridpoint via a conventional t-test. The p values across gridpoints are then sorted in ascending order, and the threshold p value for significance is calculated as $p^*_{\mathrm{FDR}} = \max_i \left[p_{(i)} : p_{(i)} \leq \frac{i}{N}\alpha_{\mathrm{FDR}}\right]$, where $\alpha_{\mathrm{FDR}} = 0.3$ is the target false discovery rate, N is the total number of points, and $p_{(i)}$ is the set of sorted p values.

For the ENSO-composite region-aggregated cutoffs, we proceed as follows. First, we compute region-aggregated cutoff rain rates for each individual JJAS. For both ENSO composites and for the composite over all years 1901-2020, the average across these yearly cutoffs is similar to the cutoffs computed across all years (compare filled circles to center of corresponding vertical lines in Fig. 2b). We therefore use the sample sizes (36 El Niño years, 41 La Niña years, 120 total years) and the interannual standard deviations in the yearly cutoffs for each region and ENSO composite to construct the 95% confidence intervals (vertical lines in Fig. 1b). These regional yearly cutoffs are reasonably normally distributed, and so we employ a standard t-test to assess the statistical significance of the correlations between the yearly cutoffs and NINO3.4. The resulting p values are $p = 0.0002$, 0.0003, 0.03, and 0.06 for AMI, CMZ, WG, and SEI, respectively.

For the risk ratios, we employ a permutation test as follows. Using our ±0.3 K threshold, there are 36 El Niño summers and 41 La Niña summers during 1901-2020. We randomly permute these 77 years and then split them into two collections, one with 36 years and the other with the remaining 41 years. We then compute the risk ratio using the collection of 36 years as the numerator and that of 41 years as the denominator. We repeat this 12,000 times and then compute the 2.5th and 97.5th percentiles across these permutations. For a given region and daily accumulation, the risk ratio is taken to significantly differ from unity if it is less than 2.5th percentile or greater than the 97.5th percentile.

Exceedance counts

The exceedance count is defined for each gridpoint, year, and daily rainfall percentile as the number of days in that year's JJAS and gridpoint exceeding the climatological rainfall at the given percentile across all years and all days of JJAS. For example, if a given year and gridpoint experienced rainfall exceeding the climatological 90th percentile on three days, the exceedance count at the 90th percentile would be three.

The exceedance count can also be applied to fixed mm day^{-1}thresholds rather than local percentiles. Fig. S4d,e,f shows the correlations vs. NINO3.4 of the yearly exceedance counts for three of the official thresholds in mm day^{-1}the India Meteorological Department uses to categorize rainfall severity.

Gamma fits to daily rainfall distributions

For each region and each ENSO-composite daily rainfall distribution, a gamma distribution was fitted for all daily accumulations > 0.1 mm using the `scipy.stats.gamma.fit` function from the SciPy package (*59*) for Python. This yields for each distribution values of the three parameters of the gamma distribution, location, shape, and scale. In the exact gamma limit, the cutoff as estimated by the method of moments is identical to the scale parameter, and we therefore take the scale parameter for each of these fits as the gamma-estimated cutoff. The ENSO risk ratios computed for the explicit gamma fits were computed from their CDFs identically to those for the empirical distributions.

Other extreme daily rainfall metrics

The block maximum daily rainfall for each JJAS is simply the single daily maximum rainfall in that JJAS at each gridpoint. We create El Niño and La Niña composite block-maxima distributions for each gridpoint by combining the block maxima across all El Niño summers or all La Niña summers into a single distribution. We then fit a Gumbel distribution to each El Niño composite and La Niña composite using the `scipy.stats.gumbel_r.fit` function, yielding for each gridpoint and composite a scale parameter value and a location parameter value. Increasing either the scale or location parameter of the Gumbel distribution increases right-tail probabilities.

Quantile regression determines the linear slope of the dependent variable (in this case, daily rainfall) vs. the independent variable (in this case, the JJAS NINO3.4 value) such that, for the specified quantile q, a fraction q of the dependent variable points fall below that line and a fraction $1 - q$ of points fall above that line (*60*). For a given JJAS, each day is assigned the JJAS-mean NINO3.4 value, and for each gridpoint all JJAS days of all years are combined into one distribution. We perform quantile regression for the 99th and 99.9th percentiles.

Pre-satellite and satellite era results

A multiple linear regression over 1901-2020 on NINO3.4 of the Central Monsoon Zone, Western Ghats, and Southeast India cutoffs yields respective weights of +1.0, +0.4, and -1.0, and the resulting timeseries is correlated with NINO3.4 for the full, pre-satellite, and satellite periods respectively at r = 0.45, 0.46, and 0.44. In the satellite era, the JJAS NINO3.4 ±0.3 K threshold results in 14 El Niño summers and 13 La Niña summers.

Motivated by concerns regarding changes in the station network for the IMD 0.25° rainfall dataset during the 1970s (*35*), we have replicated select analyses for the pre-satellite era but ending at 1969 rather than 1978. This weakly modifies the results.

ERA5 reanalysis data

Large-scale environmental fields come from the European Center for Medium-range Weather Forecasting (ECMWF) ERA5 reanalysis dataset (*40*), which provides data at hourly and monthly resolutions on a global 0.25×0.25° grid. Conveniently, over India this grid aligns identically with that of the India Meteorological Department rainfall. Though the ERA5 dataset now extends from 1950 to present, we restrict to the satellite era, 1979-2020, as the amount of observational data assimilated into the underlying numerical model increases dramatically with the availability of satellite retrievals. We compute JJAS-mean quantities from ERA5 monthly fields for June through September, and we compute daily-mean fields from ERA5 hourly fields, averaging over all 24 hourly fields.

Relative to observations, modern reanalyses show biases in the vertical thermodynamic structure (*61–63*). This is likely because space-borne retrievals of humidity encounter multiple sources of error (*64,65*). Nevertheless, given the spatial and temporal extents required for this study, no reliable

alternatives to reanalysis data exist for our purposes. And of the modern reanalysis products, ERA5 has been documented as broadly the best performing for the Indian summer monsoon sector (*66*).

B_L convective buoyancy metric

We compute the convective buoyancy metric, B_L, following (*25*) as

$$B_L \equiv g \left[w_{\text{pbl}} \frac{\theta_{e,\text{pbl}} - \theta^*_{e,\text{lft}}}{\theta^*_{e,\text{lft}}} + w_{\text{lft}} \frac{\theta_{e,\text{lft}} - \theta^*_{e,\text{lft}}}{\theta^*_{e,\text{lft}}} \right], \tag{S1}$$

where g is gravity, θ_e is equivalent potential temperature, $\theta_{e,\text{pbl}}$ is θ_e averaged over the boundary layer, θ^*_e is saturation equivalent potential temperature, $\theta_{e,\text{lft}}$ is θ_e averaged over the lower free troposphere, $\theta^*_{e,\text{lft}}$ is θ^*_e averaged over the lower free troposphere, and w_{pbl} and w_{lft} are the weights given to the undilute instability and subsaturation terms respectively. Equivalent potential temperature is computed conventionally as

$$\theta_e \equiv T \left(\frac{p_0}{p_\text{d}} \right)^{R_\text{d}/c_p} \mathcal{H}^{-R_\text{v} r_\text{v}/c_p} \exp\left(\frac{L_\text{v} r_\text{v}}{c_p T} \right), \tag{S2}$$

where T is temperature, $p_0 = 1000$ hPa is a reference pressure, p_d is the dry air partial pressure, R_d is the dry air gas constant, c_p is the specific heat of dry air at constant pressure, $\mathcal{H}$ is relative humidity, R_v is the gas constant of water vapor, and r_v is the water vapor mixing ratio. This definition neglects the contribution to θ_e of liquid water. Saturation equivalent potential temperature is computed using (S2) but setting $\mathcal{H} = 1$ and the vapor mixing ratio to its saturation value.

The layer weights are given by

$$w_{\text{pbl}} \equiv \frac{a\Delta p_{\text{pbl}}}{b\Delta p_{\text{lft}}} \ln\left(\frac{a\Delta p_{\text{pbl}} + b\Delta p_{\text{lft}}}{a\Delta p_{\text{pbl}}} \right) \tag{S3}$$

$$w_{\text{lft}} \equiv 1 - w_{\text{pbl}}, \tag{S4}$$

where a and b are parameters relating to the relative mass inflow rates in the PBL and LFT layers, respectively, and Δp_{pbl} and Δp_{lft} are the pressure thicknesses of the PBL and LFT layers, respectively. We follow (*25*) in setting $a = b = 0.5$, but we compute Δp_{pbl} and Δp_{lft} for each day and gridpoint as follows.

Following convention (*25*), we define the boundary layer to extend from the local surface pressure to 150 hPa above. To better resolve the layer boundaries and thus depths, ERA5 fields

are linearly interpolated in pressure from their native resolution (of 25 hPa spacing from 1000 to 750 hPa, 50 hPa spacing from 750 to 250 hPa, and 25 hPa spacing from 250 to 100 hPa) to 5 hPa spacing up to 200 hPa. The LFT is taken to span from the next level vertically above to the last level below the freezing level, defined as where the temperature drops below 273 K.

When computing the subcloud undilute instability term, $B_{L,\mathrm{i}}$, and the free-tropospheric subsaturation term, $B_{L,\mathrm{s}}$, individually, the layer-depth weights are included in each:

$$B_{L,\mathrm{i}} \equiv g w_{\mathrm{pbl}} \frac{\theta_{e,\mathrm{pbl}} - \theta^*_{e,\mathrm{lft}}}{\theta^*_{e,\mathrm{lft}}} \tag{S5}$$

$$B_{L,\mathrm{s}} \equiv g w_{\mathrm{lft}} \frac{\theta_{e,\mathrm{lft}} - \theta^*_{e,\mathrm{lft}}}{\theta^*_{e,\mathrm{lft}}}. \tag{S6}$$

Given our focus on extremes, we use this version of B_L in terms of equivalent potential temperatures rather than the simplified version in terms of moist enthalpies (*25*), as the latter loses some of the variations within either tail. Our use of a spatiotemporally varying PBL bounds and LFT layer thickness defined in terms of the local surface pressure and freezing level are also more involved than the original version which uses constant values of 1000 hPa as the surface pressure, 850 hPa as the PBL top, and 500 hPa as the LFT top.

ENSO risk ratios of B_L

Risk ratios for B_L, $B_{L,\mathrm{s}}$, and $B_{L,\mathrm{i}}$ components are computed identically to those for rainfall, other than being restricted to the satellite era 1979-2020. This includes restricting to rainy days and the calculation of statistical significance using a two-sided permutation test with 12,000 permuted samples at the $p < 0.05$ level.

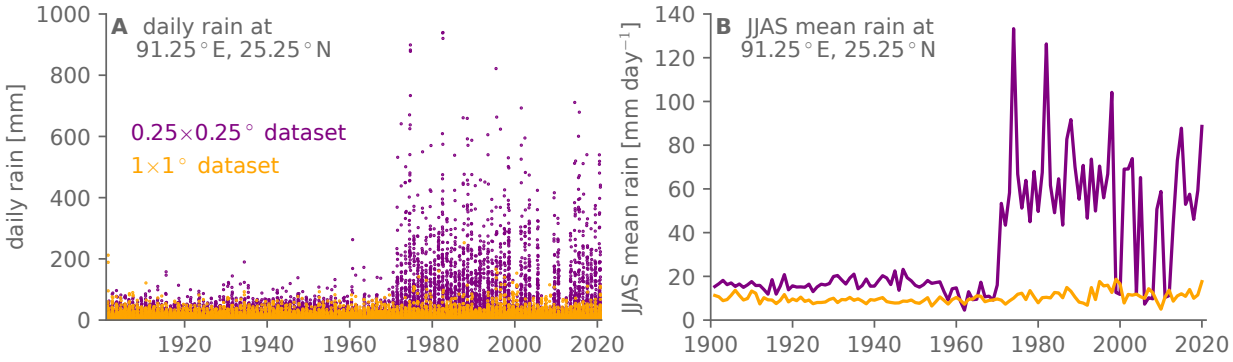

Figure S1: **Spurious values in 0.25° dataset in northeast India.** Timeseries of (a) daily and (b) JJAS-mean rain in the gridpoint encompassing 91.25°E and 25.25°N, in the 0.25×0.25° dataset in purple or the 1×1° dataset in orange. The 0.25° dataset jumps to physically implausible values in the 1970s. Other nearby gridpoints are similarly affected. This is what motivates our use of the monsoonal India mask of ref. (*31*).

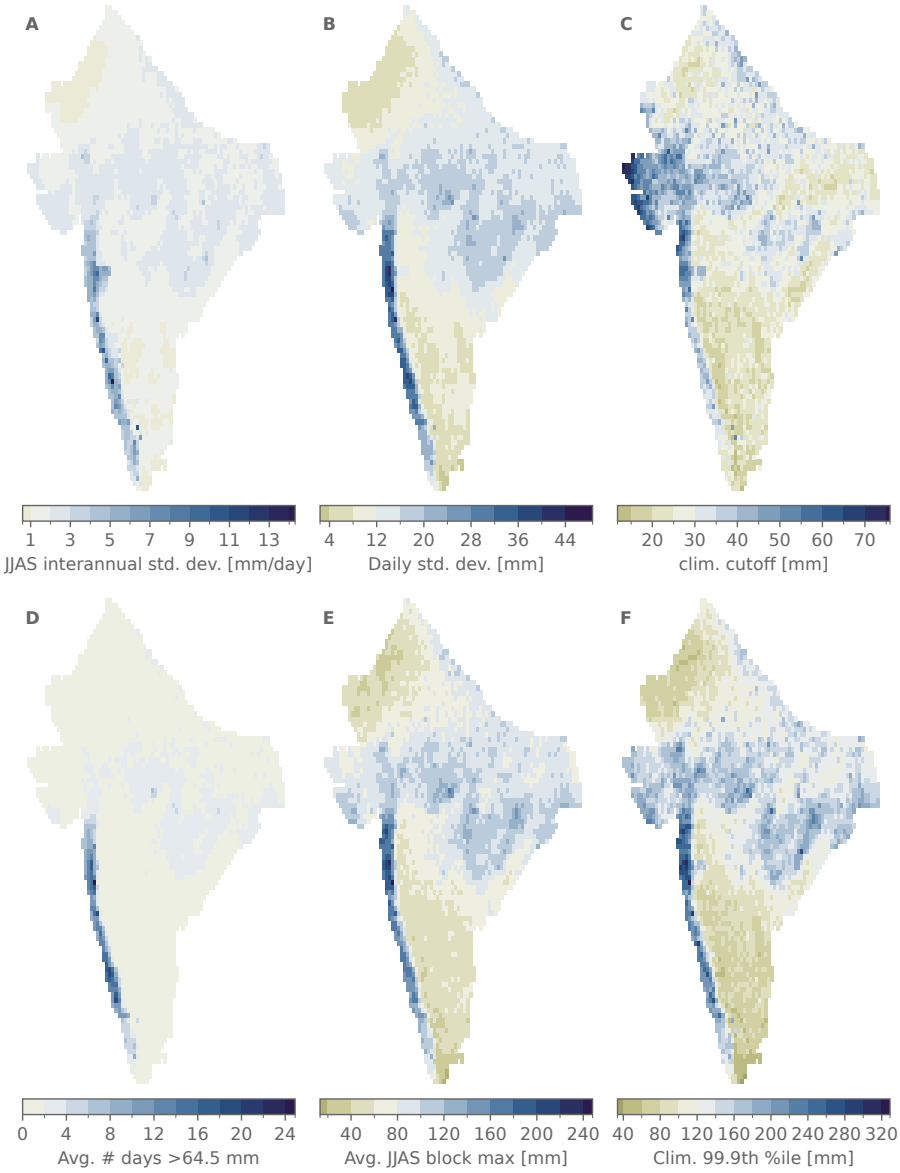

Figure S2: **Common spatial heterogeneity within India from daily to interannual timescales.** In color shading according to each colorbar, (a) JJAS-mean rainfall interannual standard deviation (units mm/day), (b) daily rainfall standard deviation (units mm), (c) climatological JJAS cutoff (units mm), (d) average number of days exceeding the India Meteorological Department's "heavy rain" threshold of 64.5 mm, (e) average across years of each year's JJAS block maximum rain (units mm), and (f) the climatological 99.9th percentile daily accumulation across all JJAS days (units mm). For each, tan shades denote values less than approximately the median across gridpoints, and blue shades denote values above that value.

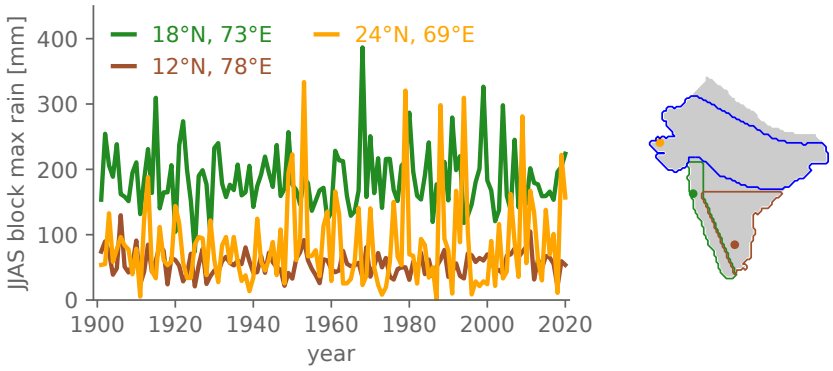

Figure S3: **Timeseries of daily rainfall block maximum within each JJAS at three representative points.** In very rainy points of WG (dark green), there are very heavy rain events nearly every summer; in dry points of SEI (brown), the heaviest events are much weaker. In Gujarat (far western CMZ; orange), most summers see modest max rainfall but occasionally receive extremely high values.

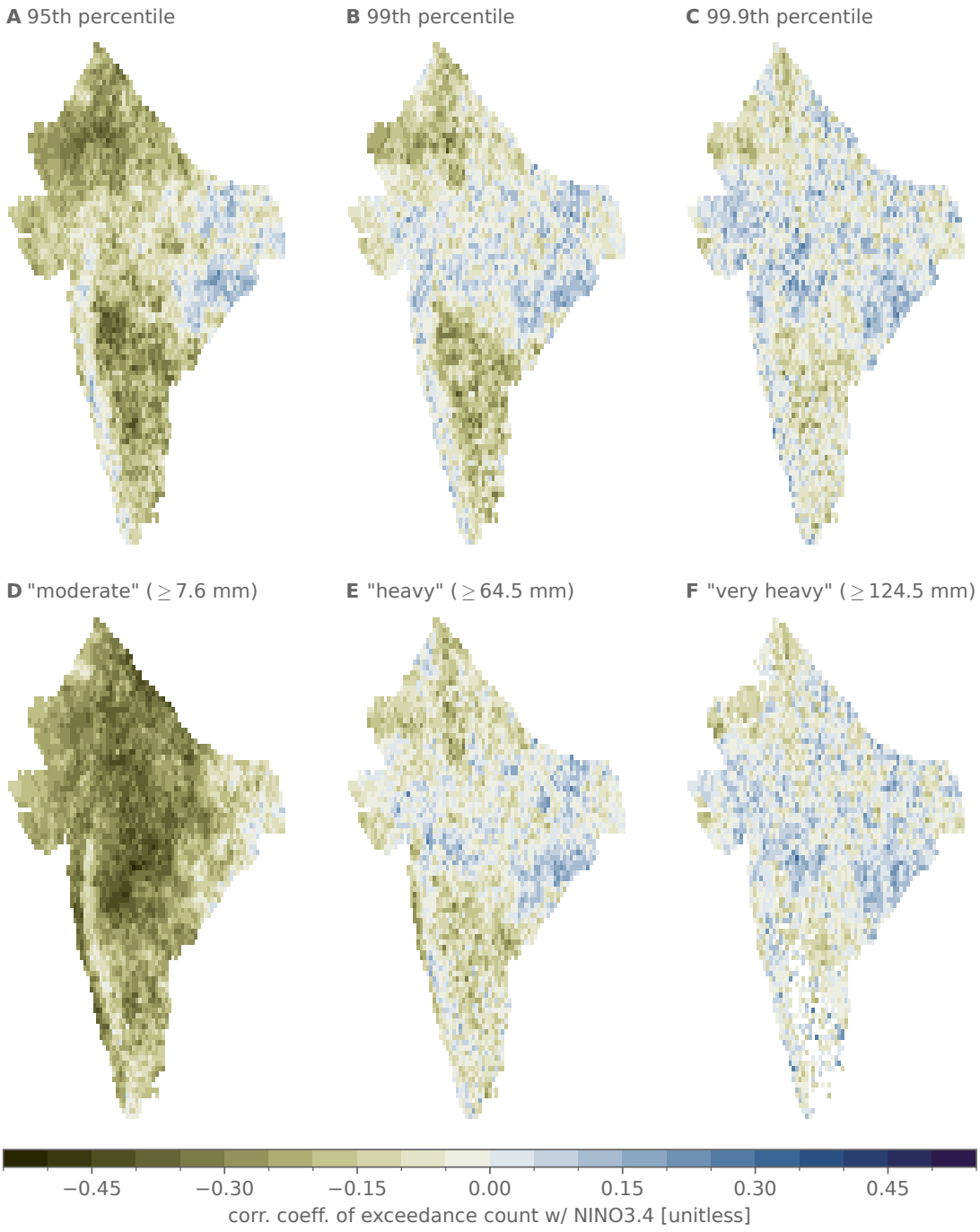

Figure S4: **Consistent results using exceedance counts as the extreme rainfall metric.** In color shading according to the colorbar, correlation coefficient of exceedance counts for each JJAS against NINO3.4 of the local climatological (a) 95th, (b) 99th, and (c) 99.9th percentile, or of the India Meteorological Department's thresholds for (d) moderate, (e) heavy, or (f) very heavy daily accumulations, with the corresponding value in mm printed in each label.

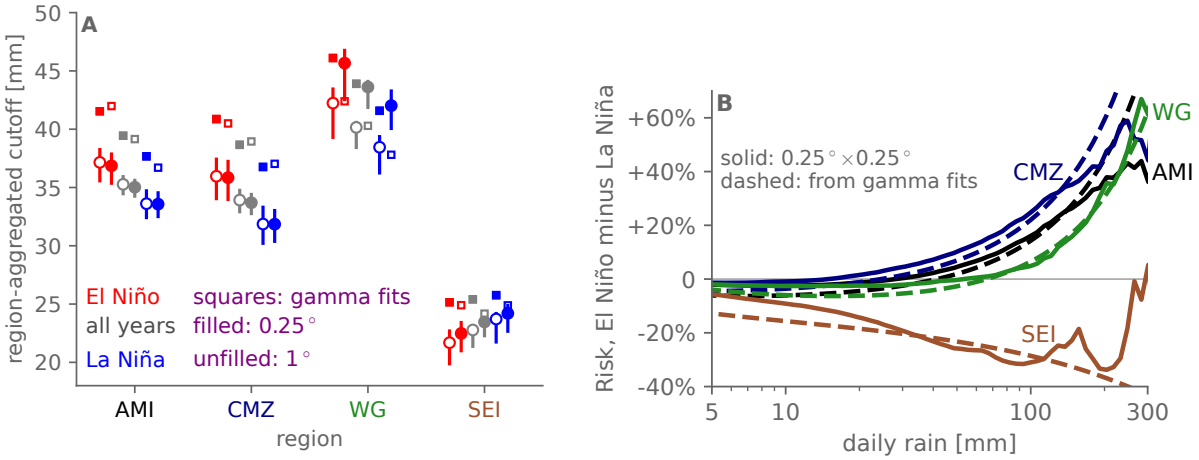

Figure S5: **Consistent results using explicit gamma fits for each region.** (a) In squares, composite regional cutoffs computed from gamma fits; all other plotted elements are identical to Fig. 2(a). (b) ENSO risk ratios of daily rainfall for each of the four monsoonal India regions according to the colors and labels. Solid curves are the actual risk ratios from the $0.25° \times 0.25°$ India Meteorological Department rainfall dataset. Dashed curves are the corresponding gamma fits.

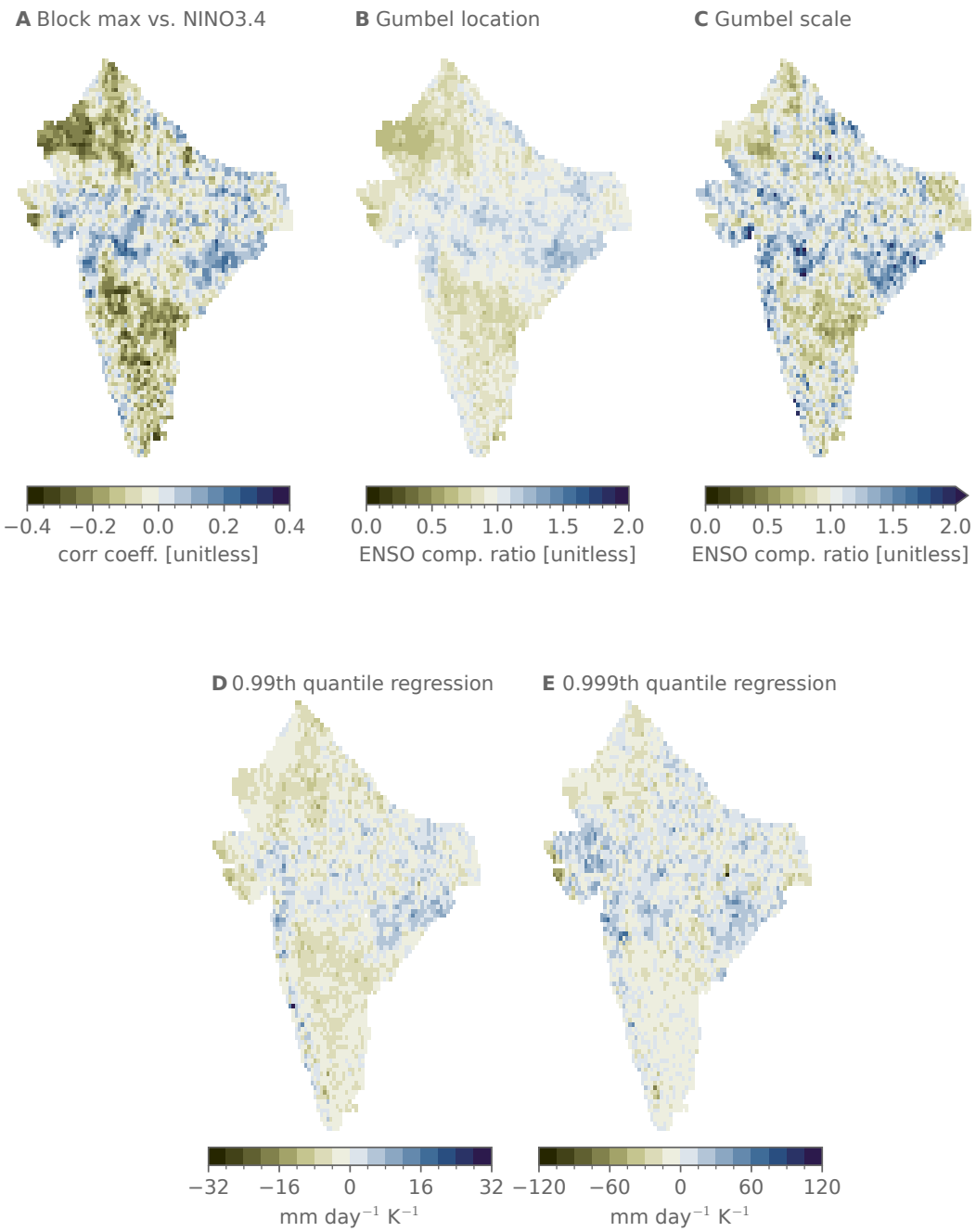

Figure S6: **Consistent results using Gumbel fits to block maxima and using quantile regression.** (a) Pearson correlation coefficient between the JJAS block maximum daily rainfall and NINO3.4, 1901-2020. (b and c) Ratio of El Niño to La Niña composite Gumbel fits to JJAS block maximum daily rainfall at each gridpoint, for the (b) location and (c) scale parameters. (d and e) Quantile regression for the (c) 99th and (d) 99.9th percentile daily rainfall (including both rainy and dry days) against NINO3.4.

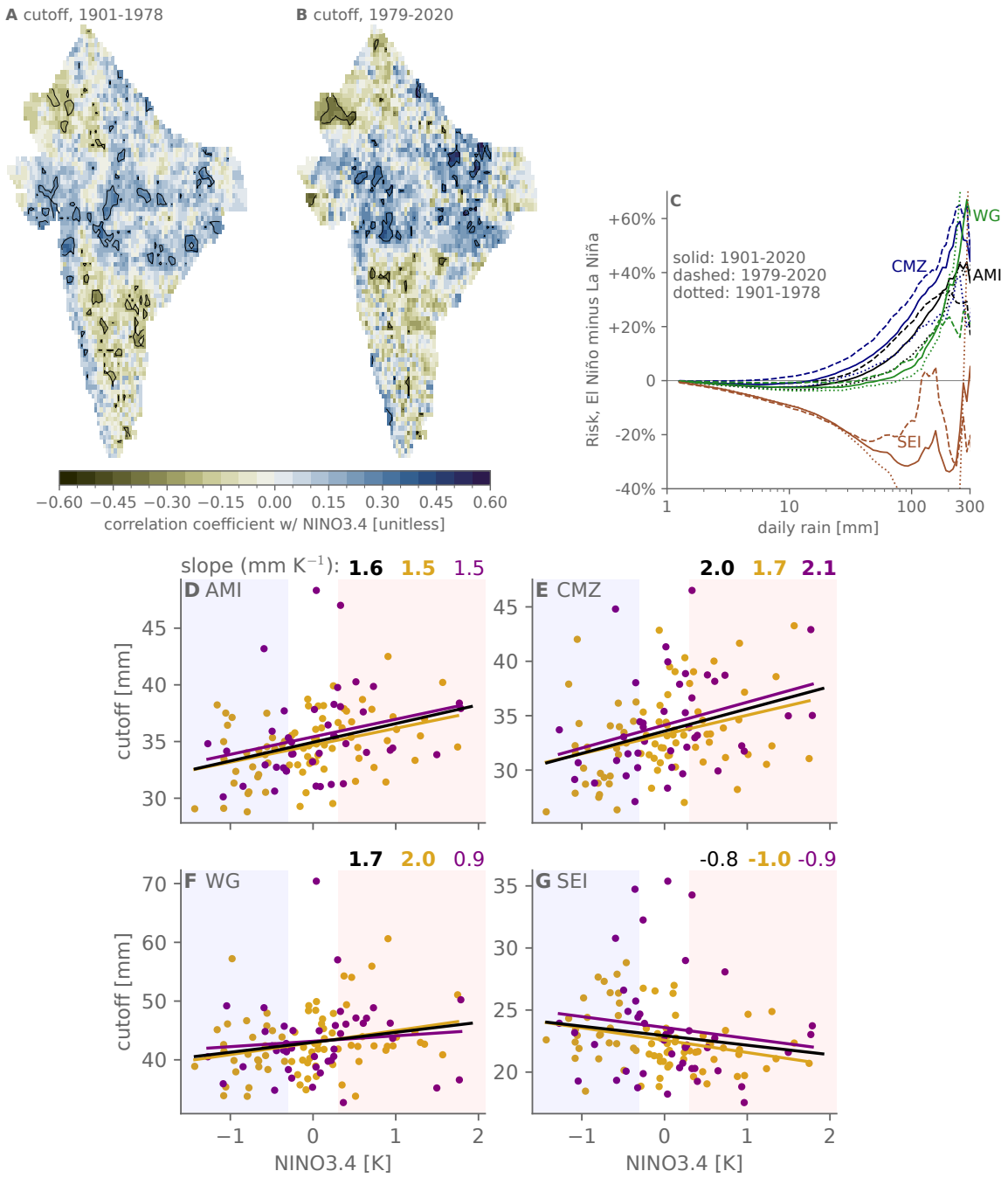

Figure S7: **Degree of consistency of results in the pre-satellite and satellite eras.** (a and b) Pointwise correlations between the JJAS cutoff and NINO3.4 restricting to (a) the pre-satellite era of 1901-1978 and (b) the satellite era of 1979-2020. Black contours enclose regions with $p < 0.05$. (c) ENSO risk ratios for each region over (solid) the full period, (dashed) the satellite era, or (dotted) pre-satellite era. [Caption continues on next page.]

Figure S7: (d through g) Scatterplots of the region-aggregated cutoff in each JJAS vs. NINO3.4, for (d) All Monsoonal India, (e) Central Monsoon Zone, (f) Western Ghats, and (g) Southeast India. Overlaid lines are corresponding linear regressions. Yellow elements are for the pre-satellite era, purple elements are for the satellite era, and black elements are for the full period. Printed values above each panel are the regression slopes for that region, in mm K^{-1}, with values in bold statistically significant at the $p = 0.05$ level. Light red and blue shading denote El Niño and La Niña conditions based on the ±0.3 K threshold used elsewhere for constructing composites. Note differing vertical axis spans across d-f.

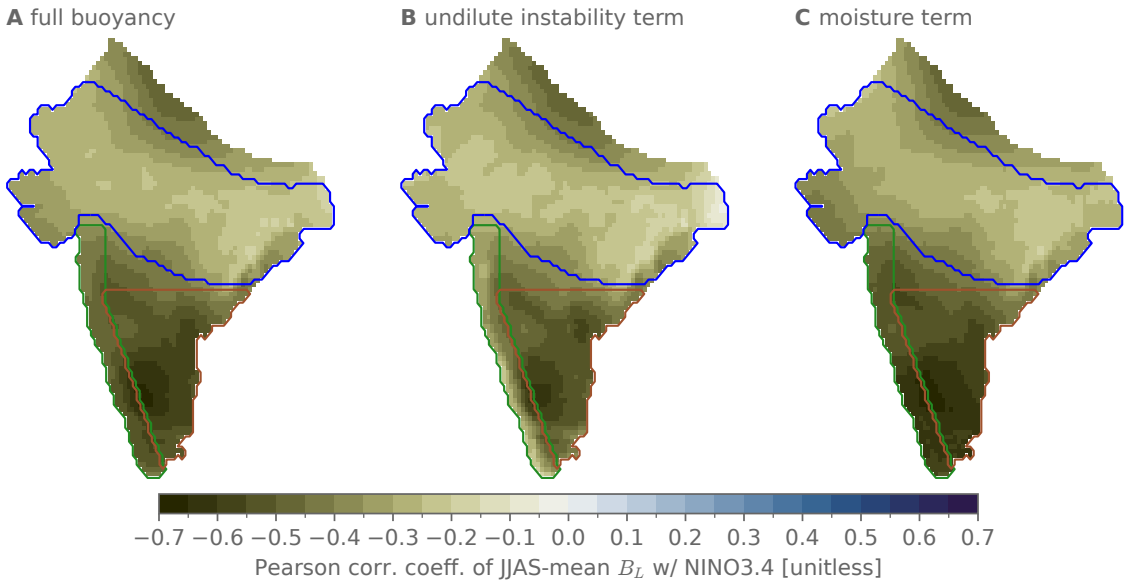

Figure S8: **JJAS-mean convective buoyancy broadly decreases with El Niño.** Pearson correlation coefficient between the JJAS-mean NINO3.4 value and the JJAS-mean values at each grid point of (A) the convective buoyancy metric, (B) the undilute instability component, and (C) the moisture component.

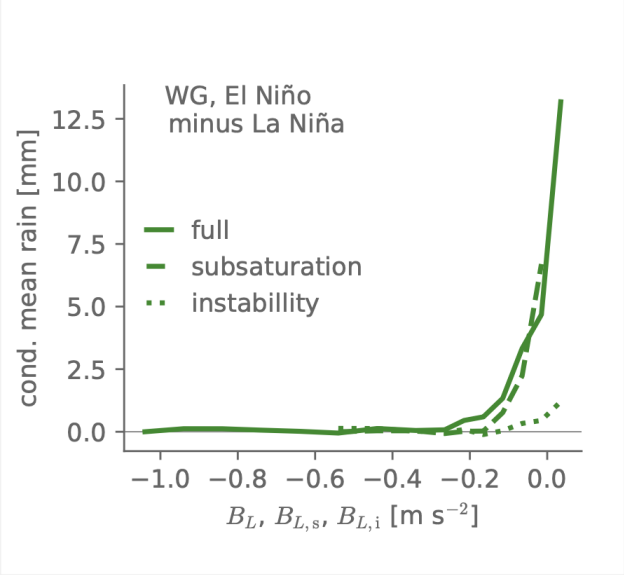

Figure S9: **In El Niño summers compared to La Niña summers, daily rainfall within the Western Ghats region tends to be even more enhanced by very moist conditions.** For grid points within the Western Ghats region, daily rainfall conditionally averaged on the full convective buoyancy metric or its individual components, restricting to El Niño years minus the same restricting to La Niña years. Solid line is for the full buoyancy metric, dashed for the moisture component, and dotted for the instability component.

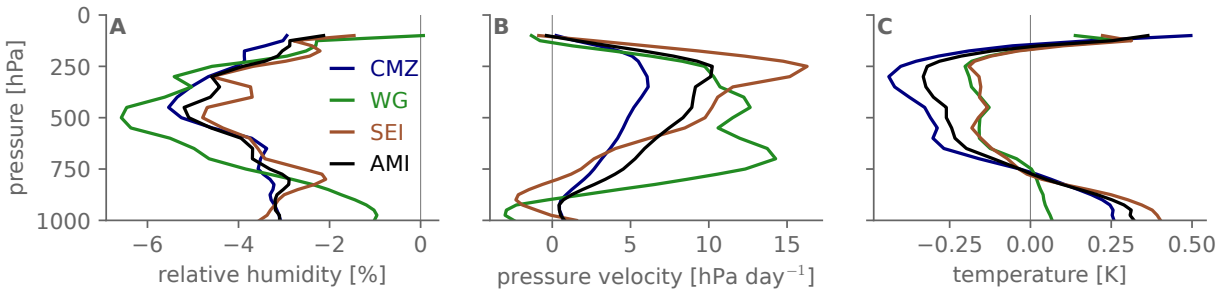

Figure S10: **JJAS-mean ENSO composite anomaly profiles.** El Niño minus La Niña, averaged over each subregion as indicated in the legend, in (a) relative humidity, (b) vertical velocity, and (c) temperature.

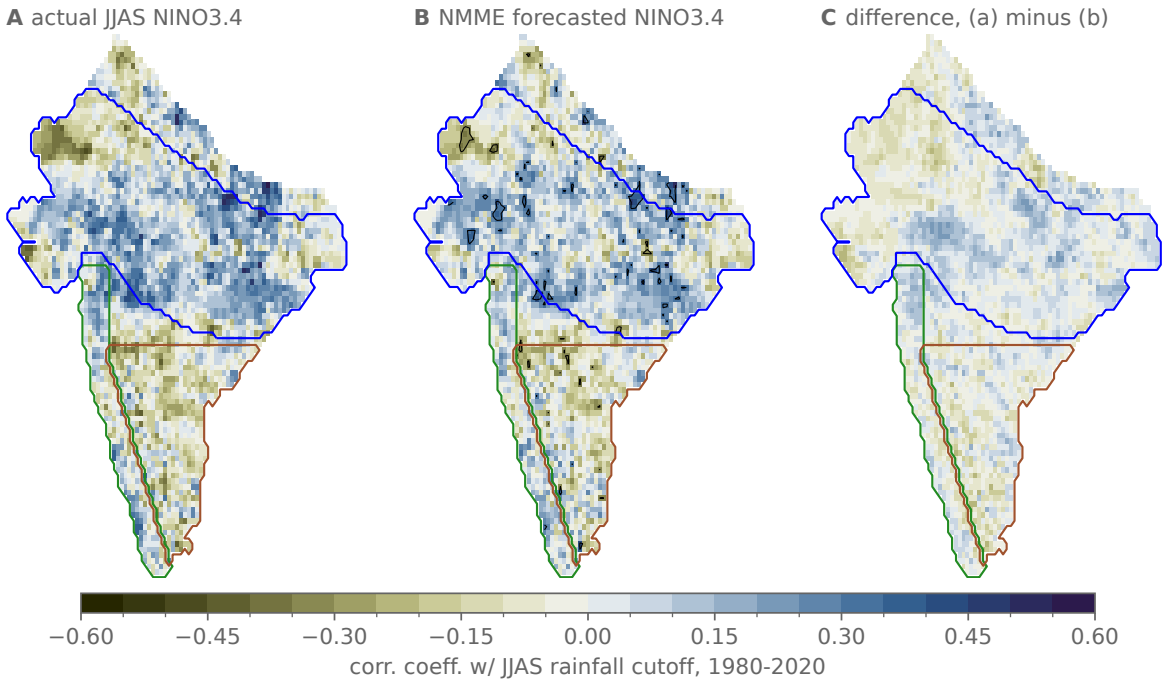

Figure S11: **Results using NINO3.4 value predicted 1 month in advance.** For the 1980-2020 period for which NMME data is available, correlation coefficient of the local JJAS cutoff vs. the JJAS NINO3.4 value computed (a) directly from ERSST, or (b) forecasted by the NMME multi-model mean of runs initialized at the preceding May 1st, with black contours enclosing regions with $p < 0.05$. Panel (c) shows their difference.

References and Notes

1. G. T. Walker, “On the Meteorological Evidence for Supposed Changes of Climate in India” (Tech. Rep., India Meteorological Department, 1910).

2. G. B. Pant, S. B. Parthasarathy, Some Aspects of an Association between the Southern Oscillation and Indian Summer Monsoon. *Arch. Meteorol. Geophys. Bioklimatol. [B]* **29**, 245–252 (1981). doi:10.1007/BF02263246

3. E. M. Rasmusson, T. H. Carpenter, The Relationship Between Eastern Equatorial Pacific Sea Surface Temperatures and Rainfall over India and Sri Lanka. *Mon. Weather Rev.* **111**, 517–528 (1983). doi:10.1175/1520-0493(1983)111<0517:TRBEEP>2.0.CO;2

4. S. Gadgil, The Indian Monsoon and Its Variability. *Annu. Rev. Earth Planet. Sci.* **31**, 429–467 (2003). doi:10.1146/annurev.earth.31.100901.141251

5. V. Moron, A. W. Robertson, D. S. Pai, On the Spatial Coherence of Sub-Seasonal to Seasonal Indian Rainfall Anomalies. *Clim. Dyn.* **49**, 3403–3423 (2017). doi:10.1007/s00382-017-3520-5

6. S. A. Hill, A. H. Sobel, M. Biasutti, M. A. Cane, On the All-India Rainfall Index and Sub-India Rainfall Heterogeneity. *Geophys. Res. Lett.* **49**, e2021GL096541 (2022). doi:10.1029/2021GL096541

7. D. L. Suhas, N. Ramesh, R. M. Kripa, W. R. Boos, Influence of Monsoon Low Pressure Systems on South Asian Disasters and Implications for Disaster Prediction. *NPJ Clim. Atmos. Sci.* **6**, 48 (2023). doi:10.1038/s41612-023-00376-5

8. S. Gadgil, S. Gadgil, The Indian Monsoon, GDP and Agriculture. *Econ. Polit. Wkly.* **41**, 4887–4895 (2006).

9. S. Curtis, A. Salahuddin, R. F. Adler, G. J. Huffman, G. Gu, Y. Hong, Precipitation Extremes Estimated by GPCP and TRMM: ENSO Relationships. *J. Hydrometeorol.* **8**, 678–689 (2007). doi:10.1175/JHM601.1

10. R. P. Allan, B. J. Soden, Atmospheric warming and the amplification of precipitation extremes. *Science* **321**, 1481–1484 (2008). doi:10.1126/science.1160787 Medline

11. J. V. Revadekar, A. Kulkarni, The El Nino-Southern Oscillation and Winter Precipitation Extremes over India. *Int. J. Climatol.* **28**, 1445–1452 (2008). doi:10.1002/joc.1639

12. A. M. Grimm, R. G. Tedeschi, ENSO and Extreme Rainfall Events in South America. *J. Clim.* **22**, 1589–1609 (2009). doi:10.1175/2008JCLI2429.1

13. X. Sun, B. Renard, M. Thyer, S. Westra, M. Lang, A Global Analysis of the Asymmetric Effect of ENSO on Extreme Precipitation. *J. Hydrol. (Amst.)* **530**, 51–65 (2015). doi:10.1016/j.jhydrol.2015.09.016

14. K. Saunders, A. G. Stephenson, P. G. Taylor, D. Karoly, The Spatial Distribution of Rainfall Extremes and the Influence of El Niño Southern Oscillation. *Weather Clim. Extrem.* **18**, 17–28 (2017). doi:10.1016/j.wace.2017.10.001

15. X.-F. Li, S. Blenkinsop, R. Barbero, J. Yu, E. Lewis, G. Lenderink, S. Guerreiro, S. Chan, Y. Li, H. Ali, R. Villalobos Herrera, E. Kendon, H. J. Fowler, Global Distribution of the

Intensity and Frequency of Hourly Precipitation and Their Responses to ENSO. *Clim. Dyn.* **54**, 4823–4839 (2020). doi:10.1007/s00382-020-05258-7

16. A. Vashisht, B. Zaitchik, Modulation of East African Boreal Fall Rainfall: Combined Effects of the Madden Julian Oscillation (MJO) and El Niño Southern Oscillation (ENSO). *J. Clim.* **35**, 2019–2034 (2021). doi:10.1175/JCLI-D-21-0583.1

17. B. N. Goswami, V. Venugopal, D. Sengupta, M. S. Madhusoodanan, P. K. Xavier, Increasing trend of extreme rain events over India in a warming environment. *Science* **314**, 1442–1445 (2006). doi:10.1126/science.1132027 Medline

18. M. Rajeevan, J. Bhate, A. K. Jaswal, Analysis of Variability and Trends of Extreme Rainfall Events over India Using 104 Years of Gridded Daily Rainfall Data. *Geophys. Res. Lett.* **35**, 2008GL035143 (2008). doi:10.1029/2008GL035143

19. S. Ghosh, D. Das, S.-C. Kao, A. R. Ganguly, Lack of Uniform Trends but Increasing Spatial Variability in Observed Indian Rainfall Extremes. *Nat. Clim. Chang.* **2**, 86–91 (2012). doi:10.1038/nclimate1327

20. C. Bajrang, R. Attada, B. N. Goswami, Possible Factors for the Recent Changes in Frequency of Central Indian Summer Monsoon Precipitation Extremes during 2005–2020. *NPJ Clim. Atmos. Sci.* **6**, 120 (2023). doi:10.1038/s41612-023-00450-y

21. V. Krishnamurthy, J. Shukla, A New Paradigm for Active–Break Cycle in the Indian Summer Monsoon. *J. Clim.* **37**, 4867–4884 (2024). doi:10.1175/JCLI-D-23-0464.1

22. S. Vishnu, W. R. Boos, P. A. Ullrich, T. A. O'Brien, Assessing Historical Variability of South Asian Monsoon Lows and Depressions With an Optimized Tracking Algorithm. *J. Geophys. Res. Atmos.* **125**, e2020JD032977 (2020). doi:10.1029/2020JD032977

23. S. Vishnu, M. D. Risser, T. A. O'Brien, P. A. Ullrich, W. R. Boos, Observed Increase in the Peak Rain Rates of Monsoon Depressions. *NPJ Clim. Atmos. Sci.* **6**, 111 (2023). doi:10.1038/s41612-023-00436-w

24. S. Dwivedi, B. N. Goswami, F. Kucharski, Unraveling the Missing Link of ENSO Control over the Indian Monsoon Rainfall. *Geophys. Res. Lett.* **42**, 8201–8207 (2015). doi:10.1002/2015GL065909

25. F. Ahmed, Á. F. Adames, J. D. Neelin, Deep Convective Adjustment of Temperature and Moisture. *J. Atmos. Sci.* **77**, 2163–2186 (2020). doi:10.1175/JAS-D-19-0227.1

26. J. D. Neelin, S. Sahany, S. N. Stechmann, D. N. Bernstein, Global warming precipitation accumulation increases above the current-climate cutoff scale. *Proc. Natl. Acad. Sci. U.S.A.* **114**, 1258–1263 (2017). doi:10.1073/pnas.1615333114 Medline

27. J. D. Neelin, C. Martinez-Villalobos, S. N. Stechmann, F. Ahmed, G. Chen, J. M. Norris, Y.-H. Kuo, G. Lenderink, Precipitation Extremes and Water Vapor. *Curr. Clim. Change Rep.* **8**, 17–33 (2022). doi:10.1007/s40641-021-00177-z

28. Materials and methods are available as supplementary material.

29. C. Martinez-Villalobos, J. D. Neelin, Why Do Precipitation Intensities Tend to Follow Gamma Distributions? *J. Atmos. Sci.* **76**, 3611–3631 (2019). doi:10.1175/JAS-D-18-0343.1

30. D. S. Pai *et al*., Development of a New High Spatial Resolution (0.25° × 0.25°) Long Period (1901-2010) Daily Gridded Rainfall Data Set over India and Its Comparison with Existing Data Sets over the Region. *Mausam* **65**, 18 (2014). doi:10.54302/mausam.v65i1.851

31. S. Gadgil, K. Rajendran, D. S. Pai, A New Rain-Based Index for the Indian Summer Monsoon Rainfall. *Mausam* **70**, 485–500 (2019). doi:10.54302/mausam.v70i3.253

32. V. Krishnamurthy, J. Shukla, Intraseasonal and Interannual Variability of Rainfall over India. *J. Clim.* **13**, 4366–4377 (2000). doi:10.1175/1520-0442(2000)013<0001:IAIVOR>2.0.CO;2

33. K. M. R. Hunt, J. K. Fletcher, The Relationship between Indian Monsoon Rainfall and Low-Pressure Systems. *Clim. Dyn.* **53**, 1859–1871 (2019). doi:10.1007/s00382-019-04744-x

34. M. Rajeevan, J. Bhate, J. D. Kale, B. Lai, "Development of a high resolution daily gridded rainll data for the Indian region" (India Meteorological Department, Met. Monograph Climatology No. 22/2005, 2005); https://apdrc.soest.hawaii.edu/doc/india_rain_ref_report.pdf.

35. M. Lin, P. Huybers, If Rain Falls in India and No One Reports It, Are Historical Trends in Monsoon Extremes Biased? *Geophys. Res. Lett.* **46**, 1681–1689 (2019). doi:10.1029/2018GL079709

36. K. K. Kumar, B. Rajagopalan, M. A. Cane, On the weakening relationship between the indian monsoon and ENSO. *Science* **284**, 2156–2159 (1999). doi:10.1126/science.284.5423.2156 Medline

37. A. Gershunov, N. Schneider, T. Barnett, Low-Frequency Modulation of the ENSO–Indian Monsoon Rainfall Relationship: Signal or Noise? *J. Clim.* **14**, 2486–2492 (2001). doi:10.1175/1520-0442(2001)014<2486:LFMOTE>2.0.CO;2

38. K. K. Kumar, B. Rajagopalan, M. Hoerling, G. Bates, M. Cane, Unraveling the mystery of Indian monsoon failure during El Niño. *Science* **314**, 115–119 (2006). doi:10.1126/science.1131152 Medline

39. F. Ahmed, J. D. Neelin, Reverse Engineering the Tropical Precipitation–Buoyancy Relationship. *J. Atmos. Sci.* **75**, 1587–1608 (2018). doi:10.1175/JAS-D-17-0333.1

40. H. Hersbach, B. Bell, P. Berrisford, S. Hirahara, A. Horányi, J. Muñoz-Sabater, J. Nicolas, C. Peubey, R. Radu, D. Schepers, A. Simmons, C. Soci, S. Abdalla, X. Abellan, G. Balsamo, P. Bechtold, G. Biavati, J. Bidlot, M. Bonavita, G. De Chiara, P. Dahlgren, D. Dee, M. Diamantakis, R. Dragani, J. Flemming, R. Forbes, M. Fuentes, A. Geer, L. Haimberger, S. Healy, R. J. Hogan, E. Hólm, M. Janisková, S. Keeley, P. Laloyaux, P. Lopez, C. Lupu, G. Radnoti, P. de Rosnay, I. Rozum, F. Vamborg, S. Villaume, J.-N. Thépaut, The ERA5 Global Reanalysis. *Q. J. R. Meteorol. Soc.* **146**, 1999–2049 (2020). doi:10.1002/qj.3803

41. D. A. Mooley, Some Aspects of Indian Monsoon Depressions and the Associated Rainfall. *Mon. Weather Rev.* **101**, 271–280 (1973). doi:10.1175/1520-0493(1973)101<0271:SAOIMD>2.3.CO;2

42. A. C. Nikumbh, A. Chakraborty, G. S. Bhat, Recent spatial aggregation tendency of rainfall extremes over India. *Sci. Rep.* **9**, 10321 (2019). doi:10.1038/s41598-019-46719-2 Medline

43. K. M. R. Hunt, A. G. Turner, P. M. Inness, D. E. Parker, R. C. Levine, On the Structure and Dynamics of Indian Monsoon Depressions. *Mon. Weather Rev.* **144**, 3391–3416 (2016). doi:10.1175/MWR-D-15-0138.1

44. D. J. Raymond, Z. Stone, S. Sentic, Rains and Showers in OTREC; Weak Temperature Gradient Modeling. *J. Adv. Model. Earth Syst.* **16**, e2023MS003980 (2024). doi:10.1029/2023MS003980

45. M. Biasutti, S. E. Yuter, Observed Frequency and Intensity of Tropical Precipitation from Instantaneous Estimates. *J. Geophys. Res. Atmos.* **118**, 9534–9551 (2013). doi:10.1002/jgrd.50694

46. M. K. Tippett, M. L. L'Heureux, E. J. Becker, A. Kumar, Excessive Momentum and False Alarms in Late-Spring ENSO Forecasts. *Geophys. Res. Lett.* **47**, e2020GL087008 (2020). doi:10.1029/2020GL087008

47. M. K. Tippett, M. Ranganathan, M. L'Heureux, A. G. Barnston, T. DelSole, Assessing probabilistic predictions of ENSO phase and intensity from the North American Multimodel Ensemble. *Clim. Dyn.* **53**, 7497–7518 (2019). doi:10.1007/s00382-017-3721-y Medline

48. B. P. Kirtman, D. Min, J. M. Infanti, J. L. Kinter III, D. A. Paolino, Q. Zhang, H. van den Dool, S. Saha, M. P. Mendez, E. Becker, P. Peng, P. Tripp, J. Huang, D. G. DeWitt, M. K. Tippett, A. G. Barnston, S. Li, A. Rosati, S. D. Schubert, M. Rienecker, M. Suarez, Z. E. Li, J. Marshak, Y.-K. Lim, J. Tribbia, K. Pegion, W. J. Merryfield, B. Denis, E. F. Wood, The North American Multimodel Ensemble: Phase-1 Seasonal-to- Interannual Prediction; Phase-2 toward Developing Intraseasonal Prediction. *Bull. Am. Meteorol. Soc.* **95**, 585–601 (2014). doi:10.1175/BAMS-D-12-00050.1

49. A. Katzenberger, J. Schewe, J. Pongratz, A. Levermann, Robust Increase of Indian Monsoon Rainfall and Its Variability under Future Warming in CMIP6 Models. *Earth Syst. Dyn.* **12**, 367–386 (2021). doi:10.5194/esd-12-367-2021

50. S. Vishnu, W. R. Boos, W. D. Collins, Historical and Future Trends in South Asian Monsoon Low Pressure Systems in a High-Resolution Model Ensemble. *NPJ Clim. Atmos. Sci.* **6**, 182 (2023). doi:10.1038/s41612-023-00502-3

51. S. A. Klein, A. Hall, Emergent Constraints for Cloud Feedbacks. *Curr. Clim. Change Rep.* **1**, 276–287 (2015). doi:10.1007/s40641-015-0027-1

52. R. S. Ajayamohan, S. A. Rao, T. Yamagata, Influence of Indian Ocean Dipole on Poleward Propagation of Boreal Summer Intraseasonal Oscillations. *J. Clim.* **21**, 5437–5454 (2008). doi:10.1175/2008JCLI1758.1

53. R. S. Ajayamohan, S. A. Rao, Indian Ocean Dipole Modulates the Number of Extreme Rainfall Events over India in a Warming Environment. *J. Meteorol. Soc. Jpn.* **86**, 245–252 (2008). doi:10.2151/jmsj.86.245

54. P. J. Borah, V. Venugopal, J. Sukhatme, P. Muddebihal, B. N. Goswami, Indian monsoon derailed by a North Atlantic wavetrain. *Science* **370**, 1335–1338 (2020). doi:10.1126/science.aay6043 Medline

55. V. Moron, R. Barbero, H. J. Fowler, V. Mishra, Storm types in India: Linking rainfall duration, spatial extent and intensity. *Philos. Trans. R. Soc. London Ser. A* **379**, 20200137 (2021). doi:10.1098/rsta.2020.0137 Medline

56. L. Dulguerov, F. Ahmed, J. D. Neelin, Extreme Tropical Precipitation Clusters Show Strong Increases in Frequency Under Global Warming in CMIP6 Models. *Geophys. Res. Lett.* **49**, e2021GL096037 (2022). doi:10.1029/2021GL096037

57. B. Huang, V. F. Banzon, E. Freeman, J. Lawrimore, W. Liu, T. C. Peterson, T. M. Smith, P. W. Thorne, S. D. Woodruff, H.-M. Zhang, Extended Reconstructed Sea Surface Temperature Version 4 (ERSST.v4). Part I: Upgrades and Intercomparisons. *J. Clim.* **28**, 911–930 (2015). doi:10.1175/JCLI-D-14-00006.1

58. D. S. Wilks, "The Stippling Shows Statistically Significant Grid Points": How Research Results Are Routinely Overstated and Overinterpreted, and What to Do about It. *Bull. Am. Meteorol. Soc.* **97**, 2263–2273 (2016). doi:10.1175/BAMS-D-15-00267.1

59. P. Virtanen, R. Gommers, T. E. Oliphant, M. Haberland, T. Reddy, D. Cournapeau, E. Burovski, P. Peterson, W. Weckesser, J. Bright, S. J. van der Walt, M. Brett, J. Wilson, K. J. Millman, N. Mayorov, A. R. J. Nelson, E. Jones, R. Kern, E. Larson, C. J. Carey, İ. Polat, Y. Feng, E. W. Moore, J. VanderPlas, D. Laxalde, J. Perktold, R. Cimrman, I. Henriksen, E. A. Quintero, C. R. Harris, A. M. Archibald, A. H. Ribeiro, F. Pedregosa, P. van Mulbregt, A. Vijaykumar, A. P. Bardelli, A. Rothberg, A. Hilboll, A. Kloeckner, A. Scopatz, A. Lee, A. Rokem, C. N. Woods, C. Fulton, C. Masson, C. Häggström, C. Fitzgerald, D. A. Nicholson, D. R. Hagen, D. V. Pasechnik, E. Olivetti, E. Martin, E. Wieser, F. Silva, F. Lenders, F. Wilhelm, G. Young, G. A. Price, G.-L. Ingold, G. E. Allen, G. R. Lee, H. Audren, I. Probst, J. P. Dietrich, J. Silterra, J. T. Webber, J. Slavič, J. Nothman, J. Buchner, J. Kulick, J. L. Schönberger, J. V. de Miranda Cardoso, J. Reimer, J. Harrington, J. L. C. Rodríguez, J. Nunez-Iglesias, J. Kuczynski, K. Tritz, M. Thoma, M. Newville, M. Kümmerer, M. Bolingbroke, M. Tartre, M. Pak, N. J. Smith, N. Nowaczyk, N. Shebanov, O. Pavlyk, P. A. Brodtkorb, P. Lee, R. T. McGibbon, R. Feldbauer, S. Lewis, S. Tygier, S. Sievert, S. Vigna, S. Peterson, S. More, T. Pudlik, T. Oshima, T. J. Pingel, T. P. Robitaille, T. Spura, T. R. Jones, T. Cera, T. Leslie, T. Zito, T. Krauss, U. Upadhyay, Y. O. Halchenko, Y. Vázquez-Baeza, SciPy 1.0 Contributors, SciPy 1.0: Fundamental algorithms for scientific computing in Python. *Nat. Methods* **17**, 261–272 (2020). doi:10.1038/s41592-019-0686-2 Medline

60. K. A. McKinnon, A. Rhines, M. P. Tingley, P. Huybers, The Changing Shape of Northern Hemisphere Summer Temperature Distributions. *J. Geophys. Res. Atmos.* **121**, 8849–8868 (2016). doi:10.1002/2016JD025292

61. R. Pincus, A. Beljaars, S. A. Buehler, G. Kirchengast, F. Ladstaedter, J. S. Whitaker, The Representation of Tropospheric Water Vapor Over Low-Latitude Oceans in (Re-)Analysis: Errors, Impacts, and the Ability to Exploit Current and Prospective Observations. *Surv. Geophys.* **38**, 1399–1423 (2017). doi:10.1007/s10712-017-9437-z

62. P. Ren, D. Kim, M.-S. Ahn, D. Kang, H.-L. Ren, Intercomparison of MJO Column Moist Static Energy and Water Vapor Budget among Six Modern Reanalysis Products. *J. Clim.* **34**, 2977–3001 (2021). doi:10.1175/JCLI-D-20-0653.1

63. B. Wolding, S. W. Powell, F. Ahmed, J. Dias, M. Gehne, G. Kiladis, J. D. Neelin, Tropical Thermodynamic-Convection Coupling in Observations and Reanalyses. *J. Atmos. Sci.* **79**, 1781–1803 (2022). doi:10.1175/JAS-D-21-0256.1

64. C. O. Ao, T. K. Meehan, G. A. Hajj, A. J. Mannucci, G. Beyerle, Lower Troposphere Refractivity Bias in GPS Occultation Retrievals. *J. Geophys. Res.* **108**, 2002JD003216 (2003). doi:10.1029/2002JD003216

65. X. Xia, D. Fu, W. Shao, R. Jiang, S. Wu, P. Zhang, D. Yang, X. Xia, Retrieving Precipitable Water Vapor Over Land From Satellite Passive Microwave Radiometer Measurements Using Automated Machine Learning. *Geophys. Res. Lett.* **50**, e2023GL105197 (2023). doi:10.1029/2023GL105197

66. S. S. Mahto, V. Mishra, Does ERA-5 Outperform Other Reanalysis Products for Hydrologic Applications in India? *J. Geophys. Res. Atmos.* **124**, 9423–9441 (2019). doi:10.1029/2019JD031155